A LightGBM-Incorporated Absorbing Boundary Conditions for the Wave-Equation-Based Meshless Method

Qi-Chang Dong, Graduate Student Member, IEEE, Zhizhang David Chen, Fellow, IEEE, Jun-Feng Wang, Member, IEEE,

Abstract—A LightGBM-Incorporated absorbing boundary condition (ABC) computation approach for the wave-equation-based the radial point interpolation meshless (RPIM) method is proposed to simulate wave propagation in open space during the computation process. Different strageties are implemented for replacing the conventional perfectly matched layers (PMLs) in the computational domain. In this work, the model is used to predict the field components on the boundary at each time step to improve computational efficiency. The effectiveness and high efficiency of our method is verified by numerical experiments.

Index Terms—wave equation, finite-difference time-domain (FDTD), neural network, perfectly matched layer (PML)

I. INTRODUCTION

Numerical methods, such as the finite-difference time-domain (FDTD) method [1] and finite element method (FEM) [2], have been extensively used for modeling electromagnetic (EM) problems. Among various numerical approaches, node-based meshless methods [3]–[7] have attracted considerable attention due to their flexibility in node distribution and independence from conventional mesh constraints.

Despite these advantages, computational domains in practical simulations must be restricted to finite sizes due to limited storage capabilities. Consequently, absorbing boundary conditions (ABCs) [8], [9] are essential to simulate continuous electromagnetic wave propagation beyond computational boundaries to minimize numerical reflections. Among numerous ABC schemes, perfectly matched layers (PMLs) [10] are widely recognized as one of the most effective and robust techniques.

In recent decades, various PML variants have been developed, including complex frequency-shifted PMLs (CFS-PMLs) [11], higher-order PMLs [12], uniaxial PMLs (UPMLs) [13] and so on. Typically, finite-thickness PMLs, usually comprising eight to ten layers, are utilized to effectively

Manuscript received xxxx; revised xxxx. This article is a preprint going to be submitted to IEEE ANTENNAS AND WIRELESS PROPAGATION LETTERS. All results and methods are solely developed by the authors. Please cite appropriately if referring to this work. It has not yet been peer-reviewed and may contain minor errors or revisions. (Corresponding author: Zhizhang David Chen)

Qi-Chang Dong is with department of Electrical and Electronic Engineering,the Hong Kong Polytechnic University and also with Eastern Institute of Technology, Ningbo, 315200, Zhejiang, P. R. China.

Zhizhang David Chen is with the Dalhousie University, Halifax, Canada. Jun-Feng Wang is with the School of Optoelectronic Engineering, Chongqing University of Posts and Telecommunications, Chongqing 400065, China.

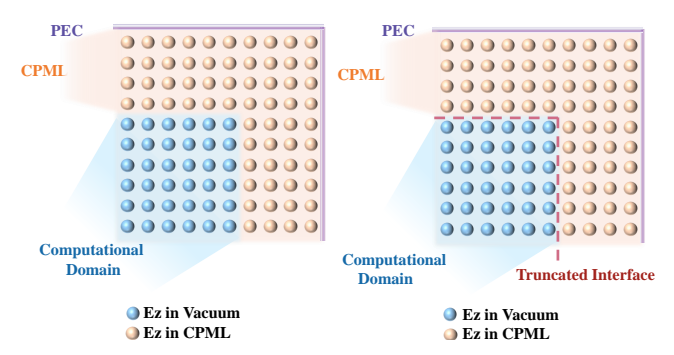


Fig. 1: Model example.(a) Original CFS-PML for meshless RPIM(b) Proposed LightGBM-Incorporated ABC:strategy 1

attenuate EM reflections. However, increasing PML thickness inevitably enlarges the computational domain, leading to significant additional memory usage and computational time. Recently, rapid advancements in artificial intelligence and machine learning have presented promising solutions for computational electromagnetic challenges [14]–[16]. According to the universal approximation theorem [17], multilayer nonlinear artificial neural networks (ANNs) possess the capability to approximate arbitrary nonlinear, continuous multidimensional functions. Due to their powerful representation and approximation capabilities, ANNs have been extensively applied to solve various complex engineering and scientific problems.

Several neural network-based PML approaches have been proposed for electromagnetic computations [18]-[21]. Unlike traditional multi-layer PML structures, these neural networkbased schemes typically require only a single computational layer, significantly reducing computational complexity, time, and memory consumption without sacrificing accuracy. For instance, a hyperbolic tangent basis function (HTBF)-based ABC model proposed in [18] efficiently predicts boundary component values at each computational step, simplifying the multi-layer PML complexity. Similarly, in [19], a gradient boosting decision tree-based PMM model has been effectively applied to FDTD methods, addressing low-frequency subsurface sensing problems. Furthermore, a hybrid model combining conventional CFS-PML with recurrent neural networks (RNNs) proposed in [21] demonstrated enhanced stability for simulation.

In this letter, one efficient LightGBM-incorporated absorbing boundary condition (ABC) computation method for the wave-equation-based radial point interpolate method is pro-

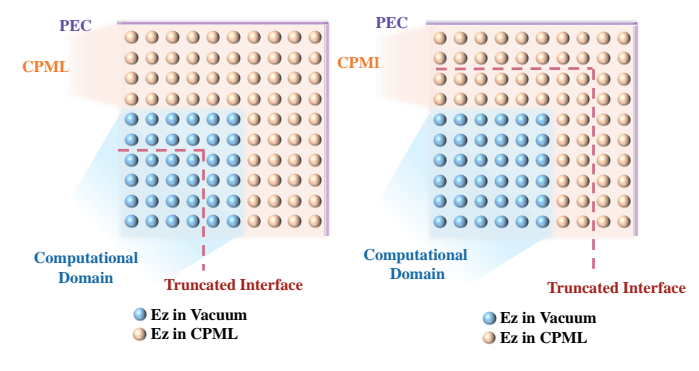


Fig. 2: Model example.(a) Proposed LightGBM-incorporated ABC: strategy 2 (b) Proposed LightGBM-incorporated ABC: strategy 3

posed to replace the traditional multi-layers PMLs. Different from previous model in [18]–[21], our proposed method uniquely focuses on wave equation-based meshless computations [22], [23], only electrical nodes are considered to compute. This innovation results in enhanced computational efficiency and novelty. The machine learning model, once trained under idealized conditions, effectively simulates wave propagation in unbounded spaces. In this study, three different strategies utilizing the proposed LightGBM-based ABC model are systematically compared with traditional CFS-PML implementations to demonstrate improved performance and efficiency.

II. METHODOLOGY

A. conventional CFS-PML for time-domain meshless method

For convenience, we define electric field nodes in the computational domain like [24]. The electric field E_z can be approximated as

$$E_z(\mathbf{r}) = \sum_{m=1}^{M} r_m(\mathbf{r}) a_m = \mathbf{R}(\mathbf{r}) \mathbf{a}$$
 (1)

where $\mathbf{r}=(x,y)$ is the coordinates of point which E_z is to be interpolated, $r_m(\mathbf{r})$ is the radial basis function associated with node m, we choose Gaussian basis function here, a_m is the coefficients to be found, and M represent the number of electric fields nodes within the support domain.

With the meshless formulation [25], (1) can be rewritten as

$$E_z^n(\mathbf{r}) = \sum_{m=1}^M \phi_m(x, y) E_{z,m}^n = \mathbf{\Phi}(\mathbf{r}) \mathbf{E}_{sz}^n(\mathbf{r})$$
 (2)

where $\mathbf{E}_{sz}(\mathbf{r})$ is the unknown electric field value vector at time step n, and the shape function vector is $\Phi(\mathbf{r}) = [\varphi_1(\mathbf{r}), \varphi_2(\mathbf{r}), \dots, \varphi_M(\mathbf{r})] = \mathbf{R}\mathbf{G}^{-1}$ with

$$\mathbf{G} = \begin{bmatrix} r_1(x_1, y_1) & \cdots & r_M(x_1, y_1) \\ r_1(x_2, y_2) & \cdots & r_M(x_2, y_2) \\ \vdots & \ddots & \vdots \\ r_1(x_M, y_M) & \cdots & r_M(x_M, y_M) \end{bmatrix}$$
(3)

The shape function $\Phi(\mathbf{r})$ should be calculated and stored before simulation , the partial derivative can be expressed [26] as

$$\frac{\partial \mathbf{\Phi}}{\partial x} = \frac{\partial \mathbf{R}}{\partial x} \mathbf{G}^{-1} \tag{4}$$

The above meshless method using Gaussian basis function has been proven to be efficient and more accurate than the FDTD method for electromagnetic modeling [27], [28].

Based on the work in [29], the transverse-magnetic case of the 2-D wave equation for electric field E_Z in a homogeneous, lossless, and source-free medium can be expressed as

$$\nabla^2 E_z - \mu \varepsilon \frac{\partial^2 E_z}{\partial t^2} = 0 \tag{5}$$

we can obtain the equation

$$E_{z,i}^{n+1} = 2E_{z,i}^n - E_{z,i}^{n-1} + \frac{\Delta t}{\mu \varepsilon} \left(A_{x2,i}^{n+\frac{1}{2}} + A_{y2,i}^{n+\frac{1}{2}} \right)$$
 (6)

we can get the final discretization formulations for ψ_{x1} and A_{x1} .

$$\psi_{x1,i}^{n+\frac{1}{2}} = c_x \sum_{m=1}^{M} E_{z,m}^{n} \frac{\partial \phi_m}{\partial x} + e^{-\alpha_x \Delta t} \psi_{x1,i}^{n-\frac{1}{2}}$$
 (7)

$$A_{x1,i}^{n+\frac{1}{2}} = A_{x1,i}^{n-\frac{1}{2}} + \frac{\Delta t}{\kappa_x} \sum_{m=1}^{M} E_{z,m}^n \frac{\partial \phi_m}{\partial x} + \Delta t \psi_{x1,i}^{n+\frac{1}{2}}$$
 (8)

where φ_m represents the shape functions of node m in the local support domain. The formulations for computing auxiliary variables A_{x2}, A_{y1} , and A_{y2} can be derived in a similar way, and results are as follows:

$$\psi_{x2,i}^{n+\frac{1}{2}} = \frac{c_x}{\Delta t} \sum_{m=1}^{M} \left(A_{x1,m}^{n+\frac{1}{2}} - A_{x1,m}^{n-\frac{1}{2}} \right) \frac{\partial \phi_m}{\partial x} + e^{-\alpha_x \Delta t} \psi_{x2,i}^{n-\frac{1}{2}}$$
(9)

$$A_{x2,i}^{n+\frac{1}{2}} = A_{x2,i}^{n-\frac{1}{2}} + \frac{1}{\kappa_x} \sum_{m=1}^{M} \left(A_{x1,m}^{n+\frac{1}{2}} - A_{x1,m}^{n-\frac{1}{2}} \right) \frac{\partial \phi_m}{\partial x} + \Delta t \psi_{x2,i}^{n+\frac{1}{2}}$$

$$\tag{10}$$

$$\psi_{y1,i}^{n+\frac{1}{2}} = c_y \sum_{m=1}^{M} E_{z,m}^n \frac{\partial \phi_m}{\partial y} + e^{-\alpha_y \Delta t} \psi_{y1,i}^{n-\frac{1}{2}}$$
(11)

$$A_{y1,i}^{n+\frac{1}{2}} = A_{y1,i}^{n-\frac{1}{2}} + \frac{\Delta t}{\kappa_y} \sum_{m=1}^{M} E_{z,m}^n \frac{\partial \phi_m}{\partial y} + \Delta t \psi_{y1,i}^{n+\frac{1}{2}}$$
 (12)

$$\psi_{y2,i}^{n+\frac{1}{2}} = \frac{c_y}{\Delta t} \sum_{m=1}^{M} \left(A_{y1,m}^{n+\frac{1}{2}} - A_{y1,m}^{n-\frac{1}{2}} \right) \frac{\partial \phi_m}{\partial y} + e^{-\alpha_y \Delta t} \psi_{y2,i}^{n-\frac{1}{2}}$$
(13)

$$A_{y2,i}^{n+\frac{1}{2}} = A_{y2,i}^{n-\frac{1}{2}} + \frac{1}{\kappa_y} \sum_{m=1}^{M} \left(A_{y1,m}^{n+\frac{1}{2}} - A_{y1,m}^{n-\frac{1}{2}} \right) \frac{\partial \phi_m}{\partial y} + \Delta t \psi_{y2,i}^{n+\frac{1}{2}}$$

$$\tag{14}$$

In summary, the computational flowchart of the proposed recursive convolutional CFS-PML computation is as follows:

- 1) Calculate the auxiliary variables ψ_{x1} and ψ_{y1} according to equations (7) and (11).
- 2) Update the auxiliary variables A_{x1} and A_{y1} based on (8) and (12).

- 3) Compute the auxiliary variables ψ_{x2} and ψ_{y2} using (9) and (13).
 - 4) Update A_{x2} and A_{y2} following (10) and (14).
 - 5) Update the electric field component E_z according to (15).
 - 6) Repeat the above steps for subsequent time steps.

Within the CFS-PML medium, the PML parameters are selected and scaled as follows:

$$\sigma_{w,i}\left(r_{w,i}\right) = \sigma_w^{\max} \left(\frac{r_{w,i}}{d}\right)^n \tag{15}$$

$$\kappa_{w,i}\left(r_{w,i}\right) = 1 + \left(\kappa_w^{\text{max}} - 1\right) \left(\frac{r_{w,i}}{d}\right)^n \tag{16}$$

$$a_{w,i}\left(r_{w,i}\right) = a_w^{\max}\left(\frac{r_{w,i}}{d}\right) \tag{17}$$

where i represents the i_{th} layer of the PML, w=x or $y,\ r_{w,i}$ is the distance between the i_th PML node and the interface between the PML medium and the computation domain, d is the thickness of the CFS-PML region, and n is the order. The choice of σ_{opt} [1], [11] is taken to be $(n+1)(150\pi\Delta s)$ where s is the nodal spacing. The CFS-PML parameters in this paper are n=4, $\sigma_{max}=2\sigma_{opt},\ k_{opt}=5$, and $a_{max}=0.05$, respectively.

B. the construction of lightGBM based absorbing boundary conditions for the Wave-Equation-Based Meshless Method

Traditional PML is often used to truncate computational domains, but often requires multiple layers such as 8 or 10 and iterative computation of intermediate variables during computation like previous $\psi_{x1}, \psi_{y1}, A_{x1}, A_{y1}, \psi_{x2}, \psi_{y2}, A_{x2}$ and A_{y2} , which raises the complexity of the computation. In practice, the parameters need to be adjusted according to the scenario to get a better result, which is very costly and time-consuming, so here we introduce neural networks, whose approximation performance has been proved in [17], to replace the multilayer PML to improve the efficiency of the computation.

Here, we have chosen to use the wave-equation corresponding to the maxwell system of equations, in which only the electric field and not the magnetic field values need to be computed.

For example, we trained two different lightGBM model for the corner cell and boundary cell, the input and output of the right boundary cell in Figure 1 is

$$\begin{cases}
x = \left[E_{z} \Big|_{i,j-1}^{s-1}, E_{z} \Big|_{i+1,j-1}^{s-1}, E_{z} \Big|_{i-1,j-1}^{s-1}, E_{z} \Big|_{i,j-1}^{s}, E_{z} \Big|_{i+1,j-1}^{s} \\
, E_{z} \Big|_{i-1,j-1}^{s}, E_{z} \Big|_{i,j}^{s-1}, E_{z} \Big|_{i+1,j}^{s-1}, E_{z} \Big|_{i-1,j}^{s-1}, E_{z} \Big|_{i,j}^{s}, E_{z} \Big|_{i+1,j}^{s} \\
, E_{z} \Big|_{i-1,j}^{s} \right] \\
y = \left[E_{z} \Big|_{i,j+1}^{s+1} \right]
\end{cases}$$
(18)

Here the s represent the s-th time step in the simulation process. And i and j is the index of X and Y coordinates, indicating x_i and y_j , respectively.

The input and output of the right corner cell in Figure 1 is

3

$$\begin{cases}
x = \left[E_{z} \Big|_{i+1,j-1}^{s-1}, E_{z} \Big|_{i+2,j-1}^{s-1}, E_{z} \Big|_{i+1,j-2}^{s-1}, E_{z} \Big|_{i+1,j-1}^{s} \\
, E_{z} \Big|_{i+2,j-1}^{s}, E_{z} \Big|_{i+1,j-2}^{s}, E_{z} \Big|_{i,j}^{s-1}, E_{z} \Big|_{i+1,j}^{s-1}, E_{z} \Big|_{i,j-1}^{s-1} \\
, E_{z} \Big|_{i,j}^{s}, E_{z} \Big|_{i+1,j}^{s}, E_{z} \Big|_{i,j-1}^{s} \right] \\
y = \left[E_{z} \Big|_{i-1,j+1}^{s+1}, E_{z} \Big|_{i-1,j}^{s+1}, E_{z} \Big|_{i,j+1}^{s+1} \right]
\end{cases} (19)$$

And in this part, three different truncation strategies can be considered, strategies 1 is truncated at the interface of computational domain and CFS-PML domain in Figure 1(b), which has been discussed extensively in [18]–[20]. The strategies 2 is an hybrid scheme in Figure 2(b) proposed by paper [21], which combines the advantage of conventional method and machine learning, has a better performance even in the late time steps. And the strategies 3 is truncated interface in the inner space in ideal space in Figure 2(a), which provides a new way to get training dataset even without the formula of traditonal PMLs.

It is worth noting that the data for strategies 1 and 2 can be collected on a traditional computational domain having 20 layers of CFS-PML [18], which means we need extra cost to obtain the dataset, while the data for strategy 3 can be collected on a sufficiently large and desirable domain, so that we can easily obtain sufficiently accurate dataset without implementing any traditional PML or any other absorbing boundary conditions.

Gradient Boosting Decision Trees (GBDT) [30] is a widely adopted tree-based machine learning algorithm. Nonetheless, their performance and scalability are often limited when applied to large-scale datasets. This limitation stems from the need to scan all data instances for each feature to calculate information gain at every possible split, a process that is highly time-consuming. Then, different strategies, including histogram-based algorithm, gradient-based one-side sampling, greedy bundling, and merge exclusive features, were proposed in LightGBM [31]. It is reported that lightGBM can accelerate the training process by up to over 20 times than GBDT while achieving almost the same accuracy [31]. Due to space limitations, only histogram-based algorithm is introduced here. For a comprehensive understanding, readers are referred to the original paper [31].

At each node, GBDT needs to compute the loss of all samples and find the optimal split point s^* :

$$s^* = \arg\min_{s} \sum_{x_i \in D_{\text{left}}} (y_i - \bar{y}_{left})^2 + \sum_{x_i \in D_{right}} (y_i - \bar{y}_{right})^2$$
(20)

LightGBM uses histogram-based optimization to speed up feature splitting. Instead of scanning all unique feature values, it groups continuous values into discrete bins, reducing computation from O(n) to O(k).

For a feature j, a histogram with k bins is built:

$$H_j(b) = \sum_{i=1}^n h(x_{ij} \in B_b)$$
 (21)

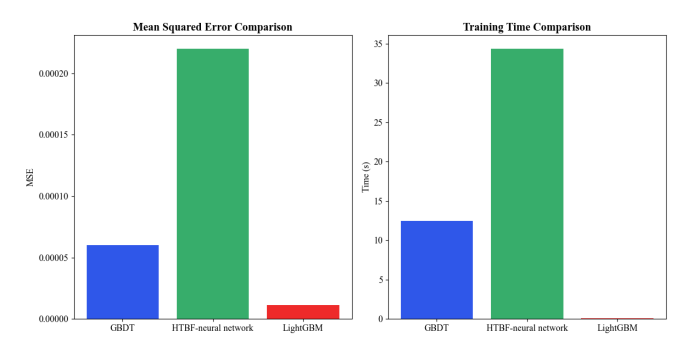


Fig. 3: MSE and training time comparison between different models

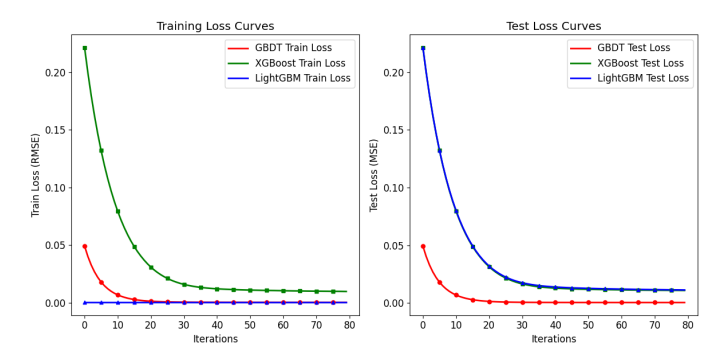


Fig. 4: Relative error of Ez at each epoch in the training process.

where $H_j(b)$ represents the number of samples in bin b. B_b is the range of values in bin b. The indicator function:

$$h(x_{ij} \in B_b) = \begin{cases} 1, & \text{if } x_{ij} \in B_b \\ 0, & \text{otherwise} \end{cases}$$
 (22)

For each bin b, LightGBM accumulates gradient G_b and Hessian H_b :

$$G_b = \sum_{x_i \in B_b} g_i, \quad H_b = \sum_{x_i \in B_b} h_i$$
 (23)

$$g_i = \frac{\partial L(y_i, F(x_i))}{\partial F(x_i)} \tag{24}$$

$$h_i = \frac{\partial^2 L(y_i, F(x_i))}{\partial F(x_i)^2} \tag{25}$$

Here g_i represent the gradient. h_i is the Hessian. LightGBM selects the best split point s^* by minimizing:

$$s^* = \arg\min_{s} \left[\frac{(G_{left})^2}{H_{left} + \lambda} + \frac{(G_{right})^2}{H_{right} + \lambda} - \frac{G_{total}^2}{H_{total} + \lambda} \right]$$
(26)

 G_{left}, G_{right} are gradient sums for left and right child nodes. H_{left}, H_{right} are Hessian sums. λ is a regularization parameter.

The mean square error is commonly used to evaluate regression tasks and it is defined as

$$MSE = \frac{1}{n} \sum_{i=1}^{n} (y_i - \hat{y}_i)^2$$
 (27)

Algorithm 1 LightGBM-based ABC Model for the Wave-Equation-Based Meshless Method

TRAINING PROCESS

Input: Training dataset $D = \{(x_i, y_i)\}_{i=1}^n$, number of trees M, max depth d, learning rate η

Initialize model with constant value: $F_0(x) = \arg\min_c \sum_{i=1}^n L(y_i, c)$, for m = 1 to M

Loop Compute first-order gradient g_i and second-order Hessian h_i

Construct histogram bins for each feature j:

$$H_j(b) = \sum_{i=1}^n 1(x_{ij} \in B_b)$$

Accumulate gradient and Hessian in each bin:

$$G_b = \sum_{x_i \in B_b} g_i, \quad H_b = \sum_{x_i \in B_b} h_i$$

Find the best split s^* by minimizing:

$$s^* = \arg\min_{s} \left[\frac{(G_{\text{left}})^2}{H_{\text{left}} + \lambda} + \frac{(G_{\text{right}})^2}{H_{\text{right}} + \lambda} - \frac{G_{\text{total}}^2}{H_{\text{total}} + \lambda} \right]$$

Grow a new leaf-wise tree $h_m(x)$ using leaf-wise splitting strategy

Update model:

$$F_m(x) = F_{m-1}(x) + \eta h_m(x)$$

Return final model $F_M(x)$

PREDICTING PROCESS

Loop

predict E_z value at every boundary cell and corner cell with trained model

Update E_z in computational domain by the Meshless method

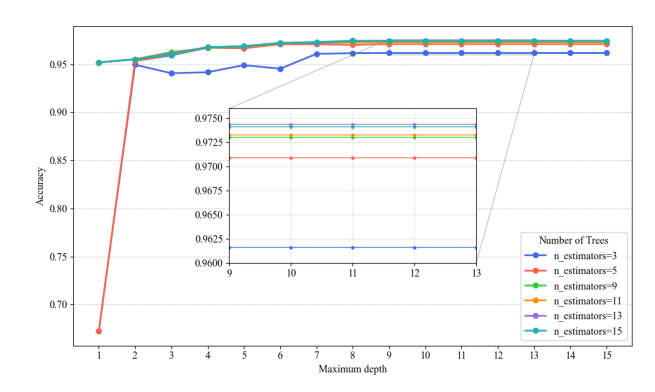


Fig. 5: Accuracy of the maximum depth of tree in the training process.

The accuracy is measured by the relative error between prediction and true value as follows:

$$Accuracy = 1.0 - \frac{\sqrt{\sum_{i=1}^{n} (y_i^2 - \hat{y}_i^2)}}{\sqrt{\sum_{i=1}^{n} y_i^2}}$$
 (28)

where y_i is the true values of Ez , \hat{y}_i is the prediction of

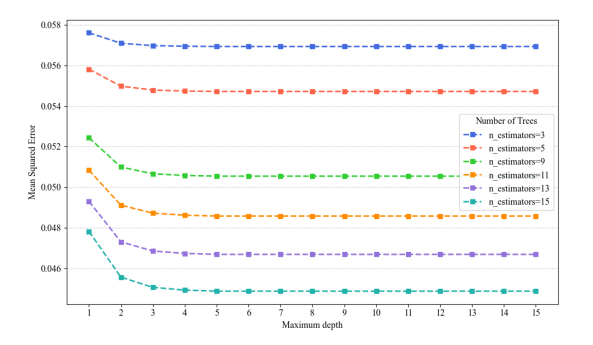


Fig. 6: The mean square error of Ez at each epoch in the training process.

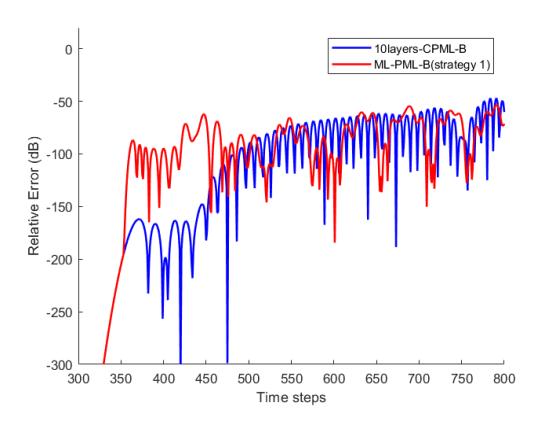


Fig. 7: Relative reflection errors among ten-cell conventional CFS-PML and proposed method of test point B.

Ez. Besides, n is the size of testing samples.

The results of training process of [19], [18], and proposed model are compared in Fig.3, whether the MSE or the training time of LightGBM is more promising than others. We also went through a series of experiments to determine the hyperparameters of the model such as the number of estimators. As shown in Fig.5 and Fig.6, the experimental results indicate that more estimators can better learn the mapping relationship in the original dataset, but too many estimators can cause overfitting and an increase in calculations. Therefore, we chose estimators number of 13 to ensure that the model has a stronger generalisation ability.

III. NUMERICAL RESULTS AND DISCUSSION

To validate the performance of the proposed scheme for the wave-equation-based meshless method, two TM-polarized current source propagation numerical experiment is conducted. The first case is to validate the performance of our proposed model with different strageties, and the second case is aimed to apply the trained model to a new scattering problem to validate the generalisation of our model while maintaining accuracy and efficiency.

A. Case 1

Without loss of generality, a wave propagation problem in an unbounded domain is considered, seen in [29]. The solution

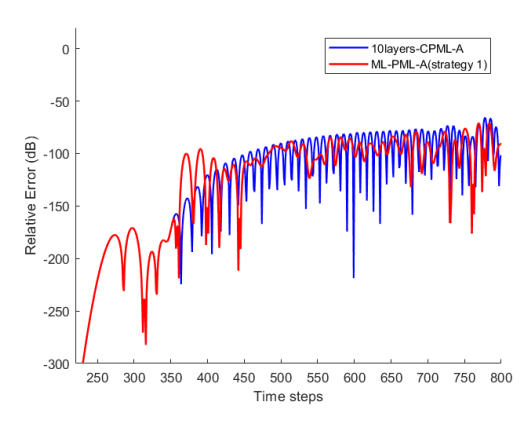


Fig. 8: Relative reflection errors among ten-cell conventional CFS-PML and proposed method of test point A.

domain of air is discretized with 101×101 uniform nodes, and the nodal spacing is $\Delta x = \Delta y = 1.5$ mm, and then t step is calculated as $\Delta t = 1$ ps. A sinusoidal pulse excited at the center of the solution domain, which can be expressed as $J_z = \sin(2\pi f_m t)$ with $f_m = 10$ GHz.

The simulated electric fields of 800 time steps are recorded at two test points within the solution domain. Test point A is located at the position one node away from the right PML; test point B is located in the top right corner of the solution domain. To evaluate the performance of the proposed method, errors are defined as

$$e(t)_{\text{dB}} = 20 \times \log_{10} \left[\left| E_z(t) - E_z^{ref}(t) \right| / \left| E_z^{ref, \text{max}} \right| \right]$$
 (29)

where E_z represent the recorded electric field component, E_z^{ref} is the reference field without any reflection effect in a big enough field, and $E_z^{ref, \max}$ is the maximum amplitude of E_z^{ref} .

As shown in Fig. 7 and Fig. 8, the relative reflection error of time-dependent electric field E_z at points A and B is shown when ten layers of conventional CFS-PML absorbing boundary conditions and the proposed model with Strategy 1 are applied. The maximum relative reflection errors at test point B for the ten-cell CFS-PML and the LightGBM-incorporated model are -47.16 dB and -53.32 dB, respectively. Similarly, at test point A, the maximum relative reflection errors are -65.56 dB and -70.85 dB, respectively. The generally lower reflection errors observed at test point A can be attributed to its greater distance from the corner of the computational domain, thereby reducing boundary-related reflections. These results demonstrate that the proposed method achieves better absorption performance with lower reflection errors. Furthermore, compared to the conventional method, our model requires less CPU time, as it only uses a single layer to truncate the computational domain.

B. Case 2

The second example is a scattering problem involving a single PEC scatterer with dimensions of 20×20 mm, located within the same computational domain. The waveforms at test points A and B, observed over 1200 time steps, are

TABLE I: Computational time (s) for different models

Methods	Structure	CPU time (s)
CFS-PML	10 layers	36.98
CFS-PML	30 layers	46.27
Proposed	1 layer	29.36

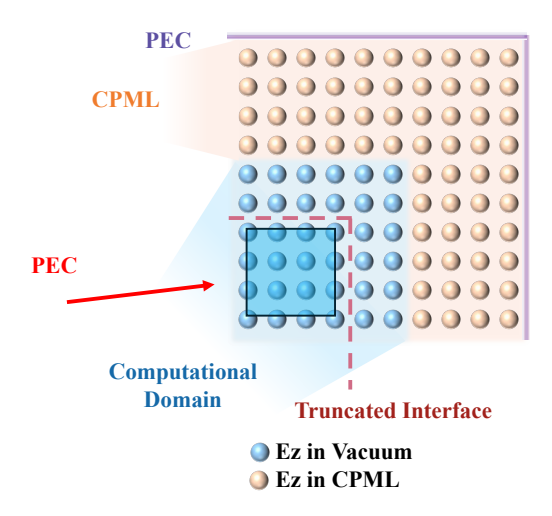


Fig. 9: Proposed ANN-Incorporated ABC

presented in Fig. 10. As shown, the waveforms produced by the proposed method with strategy 1 are in good agreement with those obtained using the conventional 10-layer CFS-PML. A comparison of the relative reflection errors between the proposed model and the conventional ten-cell CFS-PMLs is illustrated in Fig. 11.

The maximum relative reflection errors of the conventional ten-cell CFS-PML and the proposed LightGBM-based PML are -49.33 dB and -51.81 dB at test point B, and -60.31 dB and -61.89 dB at test point A, respectively. These results indicate that the proposed LightGBM-incorporated model achieves slightly better absorbing performance compared to the ten-cell conventional CFS-PML. Moreover, since the proposed method requires only one layer to truncate the computational domain, it significantly reduces CPU time consumption, as shown in Table I. In addition, the efficiency is further improved because the trained model can be reused during the computation process, which greatly reduces the overall computational resource

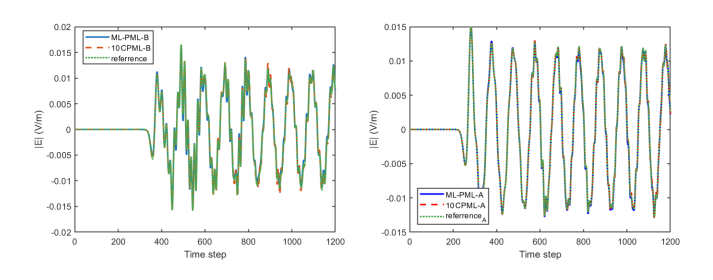
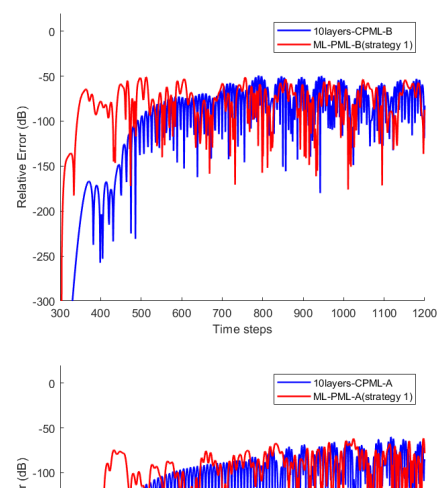


Fig. 10: Waveforms at test point A and B



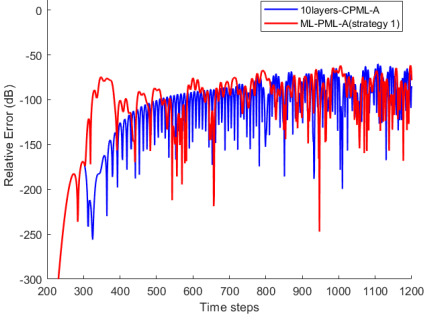


Fig. 11: Relative reflection errors among ten-cell conventional CFS-PML and proposed method of two test points

usage.

All the models are implemented on a Intel(R) Core(TM) i7-10750H CPU, time consumption may vary on different devices.

IV. CONCLUSION

In this letter, the LightGBM-incorporated CFS-PML method with three different truncation strategies applicable to wave-equation-based meshless method is proposed to improve the efficiency of the unbounded electromagnetic problems. The tree model-based LightGBM that we adopt takes less time and is more accurate in training compared to other machine learning models. The computational domain is well reduced due to the internal truncation of CFS-PML. Therefore, the proposed method not only achieves higher accuracy and efficiency with fewer layers.

REFERENCES

- A. Taflove and S. C. Hagness, Computational electrodynamics: the finitedifference time-domain method. Boston, MA, USA: Artech House, 2005.
- [2] J.-M. Jin, The Finite Element Method in Electromagnetics. New York, NY, USA: Wiley, 2002.
- [3] V. Cingoski, N. Miyamoto, and H. Yamashita, "Element-free galerkin method for electromagnetic field computations," *IEEE Transactions on Magnetics*, vol. 34, no. 5, pp. 3236–3239, 1998.
- [4] J. G. Wang and G. R. Liu, "A point interpolation meshless method based on radial basis functions," *International Journal for Numerical Methods in Engineering*, vol. 54(11), pp. 1623–1648, 2002.
- [5] S. Viana and R. Mesquita, "Moving least square reproducing kernel method for electromagnetic field computation," *IEEE Transactions on Magnetics*, vol. 35, no. 3, pp. 1372–1375, 1999.
- [6] Yu, Yiqiang and Chen, Zhizhang, "A 3-d radial point interpolation method for meshless time-domain modeling," *IEEE Transactions on Microwave Theory and Techniques*, vol. 57, no. 8, pp. 2015–2020, 2009.

- [7] Y. Yu and Z. Chen, "Towards the development of an unconditionally stable time-domain meshless method," *IEEE Transactions on Microwave Theory and Techniques*, vol. 58, no. 3, pp. 578–586, 2010.
- [8] B. Engquist and A. Majda, "Absorbing boundary conditions for the numerical simulation of waves," *Mathematics of Computation*, vol. 31, no. 139, pp. 629–651, 1977.
- [9] A. Bayliss and E. Turkel, "Radiation boundary conditions for wave-like equations," *Communications on Pure and Applied Mathematics*, vol. 33, no. 6, pp. 707–725, 1980.
- [10] J.-P. Berenger, "A perfectly matched layer for the absorption of electromagnetic waves," *Journal of Computational Physics*, vol. 114, no. 2, pp. 185–200, 1994.
- [11] J. A. Roden and S. D. Gedney, "Convolution PML (CPML): An efficient FDTD implementation of the CFS-PML for arbitrary media," *Microwave* and Optical Technology Letters, vol. 27, no. 5, pp. 334–339, 2000.
- [12] D. Correia and J.-M. Jin, "On the development of a higher-order PML," IEEE Transactions on Antennas and Propagation, vol. 53, no. 12, pp. 4157–4163, 2005.
- [13] S. D. Gedney, "An anisotropic perfectly matched layer-absorbing medium for the truncation of FDTD lattices," *IEEE Transactions on Antennas and Propagation*, vol. 44, no. 12, pp. 1630–1639, 1996.
- [14] S. Qi and C. D. Sarris, "Hybrid physics-informed neural network for the wave equation with unconditionally stable time-stepping," *IEEE Antennas and Wireless Propagation Letters*, vol. 23, no. 4, pp. 1356–1360, 2024.
- [15] Qi, Shutong and Sarris, Costas D., "Physics-informed deep operator network for 3d time-domain electromagnetic modeling," *IEEE Transactions* on Microwave Theory and Techniques, pp. 1–13, 2024.
- [16] L. Guo, M. Li, S. Xu, F. Yang, and L. Liu, "Electromagnetic modeling using an fdtd-equivalent recurrent convolution neural network: Accurate computing on a deep learning framework," *IEEE Antennas and Propa*gation Magazine, vol. 65, no. 1, pp. 93–102, 2023.
- [17] M.-X. Wang and Y. Qu, "Approximation capabilities of neural networks on unbounded domains," *Neural Networks*, vol. 145, pp. 56–67, 2022. [Online]. Available: https://www.sciencedirect.com/science/article/pii/ S0893608021003920
- [18] H. M. Yao and L. Jiang, "Machine-learning-based PML for the FDTD method," *IEEE Antennas and Wireless Propagation Letters*, vol. 18, no. 1, pp. 192–196, 2019.
- [19] N. Feng, H. Wang, Z. Zhu, Y. Zhang, L. Yang, and Z. Huang, "Gradient boosting decision tree-based PMM model integrated into FDTD method for solving subsurface sensing problems," *IEEE Transactions on Antennas and Propagation*, vol. 72, no. 7, pp. 5892–5899, 2024.
- [20] N. Feng, Y. Chen, Y. Zhang, M. S. Tong, Q. Zeng, and G. P. Wang, "An expedient DDF-based implementation of perfectly matched monolayer," *IEEE Microwave and Wireless Components Letters*, vol. 31, no. 6, pp. 541–544, 2021.
- [21] H.-Y. Ren, X.-H. Wang, T. Wei, and L. Wang, "Recurrent neural network-assisted truncation of convolutional perfectly matched layers for fdtd," *IEEE Antennas and Wireless Propagation Letters*, vol. 23, no. 5, pp. 1493–1497, 2024.
- [22] J. Wang, Z. Chen, J. Liang, Y. Wu, C. Peng, S. Tao, and J. Li, "The split-field pml absorbing boundary condition for the unconditionally stable node-based lod-rpim method," *IEEE Antennas and Wireless Propagation Letters*, vol. 17, no. 10, pp. 1920–1924, 2018.
- [23] J.-F. Wang, G. Li, and Z. Chen, "Convolutional implementation and analysis of the cfs-pml abc for the fdtd method based on wave equation," *IEEE Microwave and Wireless Components Letters*, vol. 32, no. 7, pp. 811–814, 2022.
- [24] A. Cangellaris, C.-C. Lin, and K. Mei, "Point-matched time domain finite element methods for electromagnetic radiation and scattering," *IEEE Transactions on Antennas and Propagation*, vol. 35, no. 10, pp. 1160–1173, 1987.
- [25] Y. Yu and Z. Chen, "The cpml absorbing boundary conditions for the unconditionally stable meshless modeling," *IEEE Antennas and Wireless Propagation Letters*, vol. 11, pp. 468–472, 2012.
- [26] T. Kaufmann, C. Fumeaux, and R. Vahldieck, "The meshless radial point interpolation method for time-domain electromagnetics," in 2008 IEEE MTT-S International Microwave Symposium Digest, 2008, pp. 61–64.
- [27] S. Yang, Z. Chen, Y. Yu, and S. Ponomarenko, "On the numerical dispersion of the radial point interpolation meshless method," *IEEE Microwave and Wireless Components Letters*, vol. 24, no. 10, pp. 653–655, 2014.
- [28] S. Yang, Y. Yu, Z. Chen, and S. Ponomarenko, "A time-domain collocation meshless method with local radial basis functions for electromagnetic transient analysis," *IEEE Transactions on Antennas and Propagation*, vol. 62, no. 10, pp. 5334–5338, 2014.

- [29] J.-F. Wang, Z. D. Chen, C. Peng, J. Li, and S. A. Ponomarenko, "Development of the recursive convolutional cfs-pml for the waveequation-based meshless method," *IEEE Transactions on Antennas and Propagation*, vol. 69, no. 6, pp. 3599–3604, 2021.
- [30] J. H. Friedman, "Greedy function approximation: A gradient boosting machine." *The Annals of Statistics*, vol. 29, no. 5, pp. 1189 1232, 2001. [Online]. Available: https://doi.org/10.1214/aos/1013203451
- [31] G. Ke, Q. Meng, T. Finley, T. Wang, W. Chen, W. Ma, Q. Ye, and T.-Y. Liu, "Lightgbm: A highly efficient gradient boosting decision tree," in *Neural Information Processing Systems*, 2017. [Online]. Available: https://api.semanticscholar.org/CorpusID:3815895